Journal of Computational Physics 229 (2010) 875–889

Contents lists available at ScienceDirect

Journal of Computational Physics

journal homepage: www.elsevier.com/locate/jcp

Efficient symmetric discretization for the Poisson, heat and Stefan-type problems with Robin boundary conditions

Joseph Papac [a,*], Frédéric Gibou [a,b], Christian Ratsch [c]

[a] Mechanical Engineering Department, University of California, Santa Barbara, CA 93106, United States
[b] Computer Science Department, University of California, Santa Barbara, CA 93106, United States
[c] Department of Mathematics, and Institute for Pure and Applied Mathematics, University of California, Los Angeles, CA 90095, United States

ARTICLE INFO

Article history:
Received 23 April 2009
Received in revised form 18 August 2009
Accepted 10 October 2009
Available online 17 October 2009

Keywords:
Level set method
Robin boundary condition
Stefan
Poisson
Diffusion
Irregular domains

ABSTRACT

We present a novel and efficient method for solving the Poisson equation, the heat equation, and Stefan-type problems with Robin boundary conditions over potentially moving, arbitrarily-shaped domains. The method utilizes a level set framework, thus it has all of the benefits of a sharp, implicitly-represented interface such as the ease of handling complex topological changes. This method is straightforward to implement and leads to a linear system that is symmetric and positive definite, which can be inverted efficiently with standard iterative methods. This approach is second-order accurate for both the Poisson and heat equations, and first-order accurate for the Stefan problem. We demonstrate the accuracy in the L^1 and L^∞ norms.

1. Introduction

The Poisson and heat equations on irregular domains and their extension to moving boundary, or Stefan problems, are central to countless applications in science and engineering. Examples include the design of solidification methodologies for advanced materials in the aerospace and semiconductor industries, combustion, bio-nanotechnology, tissue engineering, bacteria colonies (which can be used in the development of drugs) and many others. Several schemes have been proposed to numerically compute solutions to these equations. Finite element methods [24,30] have achieved very good results, however in the case of moving boundaries, the need for remeshing makes the method computationally expensive, especially in three spatial dimensions. Boundary integral methods [2] have also been successful and probably the most efficient for 2D diffusion dominated problems. In fact, the earliest level set approach for solidification problems [33] used a boundary integral approach. A difficulty with this approach is that it is complex to implement in three spatial dimensions. Chen et al. [5] proposed a simple level set method in an Eulerian coordinate system for solving Stefan problems with Dirichlet boundary conditions applied at the boundary of the moving front. In this formulation, the entire solution process is based on a fixed Cartesian grid. Similar work can also be found in [35]. This type of discretization when applied to a time-implicit method leads to a non-symmetric linear system. Improvements were made to this method including a second-order accurate approach with a symmetric linear system [11], and later a fourth-order accurate approach [12]. All of these schemes have considered Dirichlet boundary conditions only.

* Corresponding author.
E-mail address: jepapac@gmail.com (J. Papac).

0021-9991/$ - see front matter © 2009 Elsevier Inc. All rights reserved.
doi:10.1016/j.jcp.2009.10.017

However, there exist applications and corresponding models for which the inherent physics require a more general Robin boundary condition on a possibly moving, irregular domain. For example, an application that has received considerable interest is the modeling of thin film growth by molecular beam epitaxy (MBE), one of the main processes used in the semiconductor industry. In the case of MBE, the diffusion of adatoms on the substrate, their nucleations and the subsequent growth of islands can be modeled by an Island Dynamics approach (a Stefan-type problem) based on the level set method, as first proposed by Caflisch et al. [3]. A distinguishing feature of this model is that it employs coarse-graining in the lateral directions while retaining atomistic discreteness in the growth direction, so that it is capable of describing large nanoscale surface structures. So far, such models have only considered equilibrium adatom densities at the islands' boundaries, i.e. Dirichlet boundary conditions. The physical assumption behind this boundary condition is the absence of current of adatoms between different growth layers. However, it is well known that for most systems there is an energy barrier for atoms to diffuse between different layers, the so-called Ehrlich–Schwoebel barrier [6,31]. This additional barrier effectively leads to an uphill current and promotes the roughening of the surface and the formation of mounds [36]. In a microscopic picture, such a barrier and its strain-induced spatial variations are the driving force for the formation of quantum dots, three-dimensional structures well known for their important opto-electronic properties. The modeling of the barrier for adatoms to diffuse between different layers has been proposed several decades ago in [36] and appears as a Robin boundary condition for continuum-based models.

The Island Dynamics model is based on the level-set formulation [27,32,25]. Two of the main advantages of the level set formulation is the fact that (1) it is a sharp interface model, thus it can be used to precisely locate the interface in order to apply discretizations that depend on the exact interface location, as is the case in typical Stefan-type problem; (2) only the standard time step restrictions for stability and consistency are required, making the method more efficient than other implicit methods such as the phase-field approach [18,16,17,21,30,15]. Level set methods have been extremely successful on uniform Cartesian grids in the study of physical problems such as compressible flows, incompressible flows, multiphase flows (see e.g. [25,32] and the references therein), epitaxial growth (see e.g. [3,13,14,28] and the references therein) and in image processing (see e.g. [26] and the references therein). However, level set methods have limitations of their own: boundary conditions are not straightforward to impose, unlike in phase-field methods for example. Progress has been made in the level set community with the advent of the ghost-fluid method [7,11,12,22,4,8]. However, solving a diffusion-type problem on moving irregular domains with a Robin boundary condition has so far resisted every attempt in the level set community.

In this paper, we present an efficient Eulerian numerical method to solve the Stefan problem with Robin boundary conditions imposed on a possibly moving, irregular domain. In particular, this method is implicit in time to avoid the stringent time step restriction associated with explicit schemes and leads to symmetric positive definite linear systems that can be inverted efficiently with iterative methods such as the preconditioned conjugate gradient method [29]. We use a dimension-by-dimension approach on a fixed Cartesian grid, making the extension of the method to three spatial dimensions straightforward. This approach achieves second-order accurate solutions to the Poisson and heat equations, and first-order accurate solutions to the Stefan problem.

We describe the main components of the level set method in Section 2. We then present the algorithm to impose Robin boundary conditions for the Poisson and heat equations in Section 3 and for the Stefan problem in Section 4. Section 5 presents numerical results for the Poisson, heat and Stefan problems. We conclude in Section 6.

2. Interface tracking – the level set method

In this paper, we use the level set method [27] to implicitly represent the moving boundary. Consider a domain $\Omega = \Omega^- \cup \Omega^+$ with boundary $\partial\Omega$, separated by a lower dimensional interface Γ. We describe Ω^- by the set of points, $\mathbf{x}$, such that $\phi(\mathbf{x}) < 0$. Likewise, we describe Ω^+ by the set of points such that $\phi(\mathbf{x}) > 0$. The interface Γ is implicitly defined by $\phi(\mathbf{x}) = 0$. The evolution of the interface is then given by the evolution of ϕ, and obeys:

$$\phi_t + \mathbf{V} \cdot \nabla\phi = 0, \tag{1}$$

where $\mathbf{V}$ is an externally generated velocity field.

The normal to the interface and the interface mean curvature are defined by

$$\mathbf{n} = \frac{\nabla\phi}{|\nabla\phi|}, \quad \kappa = \nabla \cdot n, \tag{2}$$

respectively and are numerically approximated by central differencing. In order to keep the level set function close to a signed distance function, we use the reinitialization scheme of Sussman et al. [34]:

$$\phi_\tau + \mathrm{Sign}(\phi_0)(|\nabla\phi| - 1) = 0, \tag{3}$$

for a few iterations in fictitious time, τ. Here ϕ_0 is a level set function that is not necessarily a signed distance function but describes the same contour as that of ϕ. The interested reader is referred to [25,32] for general details of the level set method.

3. Numerical approach

3.1. Numerical approach for the Poisson and heat equations

Our approach utilizes a uniform cell-based discretization of the domain with the discrete values located at the cell centers, as shown in Fig. 1. We first consider the heat equation, noting that the case of the Poisson equation is a trivial subset. Consider the heat equation applied to the interior region Ω^-,

$$\rho_t - k\Delta\rho = g, \tag{4}$$

with a Robin boundary condition on Γ,

$$\nabla\rho\cdot\mathbf{n} + \alpha\rho = f. \tag{5}$$

We will express the heat equation in integral form,

$$\int_{\Omega^-}\rho_t\,dA - \int_{\Omega^-}k\Delta\rho\,dA = \int_{\Omega^-}g\,dA, \tag{6}$$

and apply the Crank–Nicolson finite difference scheme to (6) over each grid cell, $\mathcal{C}_{ij}$,

$$\int_{\mathcal{C}_{ij}\cap\Omega^-}\left(\rho_{ij}^{n+1} - \rho_{ij}^{n} - \frac{k\Delta t}{2}\widetilde{\Delta}\rho^{n+1} - \frac{k\Delta t}{2}\widetilde{\Delta}\rho^{n} - \frac{\Delta t}{2}g_{ij}^{n+1} - \frac{\Delta t}{2}g_{ij}^{n}\right)dA = 0, \tag{7}$$

where $\widetilde{\Delta}$ represents a discretization for the Laplacian.

For the evaluation of the terms in (7), consider the general case of a cell in which the interface Γ passes through, as seen in Fig. 1. The first and second terms in (7) are straightforward to evaluate if we make the reasonable approximation that ρ is spatially constant within each grid cell, i.e.,

$$\int_{\mathcal{C}_{ij}\cap\Omega^-}\rho\,dA = \rho_{ij}\cdot\mathrm{Area}_{\mathcal{C}_{ij}\cap\Omega^-}.$$

Similarly, the last two terms in (7) are straightforward to evaluate if we approximate g as constant within the grid cell,

$$\int_{\mathcal{C}_{ij}\cap\Omega^-}g\,dA = g_{ij}\cdot\mathrm{Area}_{\mathcal{C}_{ij}\cap\Omega^-}.$$

Now consider the third and fourth terms in (7). We will apply the divergence theorem to each of these terms in order to evaluate the flux through the boundaries of our region of interest,

$$\int_{\mathcal{C}_{ij}\cap\Omega^-}\nabla\cdot\nabla\rho\,dA = \int_{\partial(\mathcal{C}_{ij}\cap\Omega^-)}\nabla\rho\cdot\mathbf{n}\,dl.$$

We can split this integral into two parts: one part contains the grid cell boundary ($\partial\mathcal{C}_{ij}\cap\Omega^-$, shown as the bold solid segments in Fig. 1) the second part contains the interface boundary ($\mathcal{C}_{ij}\cap\Gamma$, shown as the bold dashed segment in Fig. 1)

$$\int_{\partial(\mathcal{C}_{ij}\cap\Omega^-)}\nabla\rho\cdot\mathbf{n}\,dl = \int_{\partial\mathcal{C}_{ij}\cap\Omega^-}\nabla\rho\cdot\mathbf{n}\,dl + \int_{\mathcal{C}_{ij}\cap\Gamma}\nabla\rho\cdot\mathbf{n}\,dl. \tag{8}$$

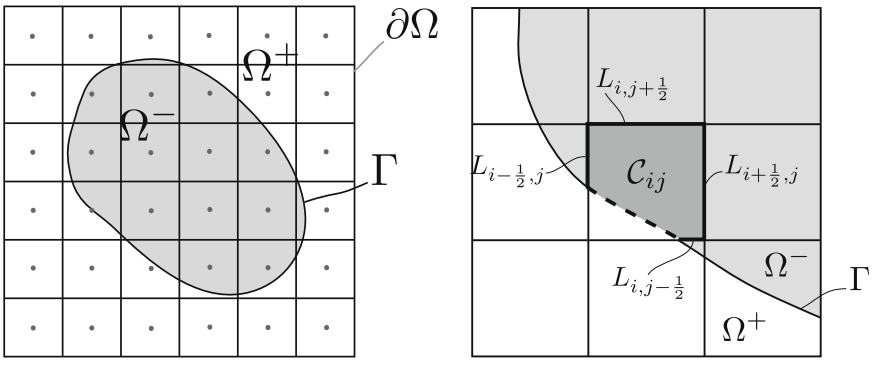

Fig. 1. Cell-based discretization of the domain (left), and cell cut by the interface (right).

On the first term of the right hand side of (8), we can apply a standard finite difference approximation of the gradient since the normals are precisely aligned with the cartesian grid. The integration along the cell boundary can be performed piecewise, therefore, the general case is given by,

$$\int_{\partial\mathcal{C}_{ij}\cap\Omega^-} \nabla\rho\cdot\mathbf{n}\,dl = \frac{\rho_{i+1,j}-\rho_{ij}}{\Delta x}L_{i+\frac{1}{2}j} - \frac{\rho_{ij}-\rho_{i-1,j}}{\Delta x}L_{i-\frac{1}{2}j} + \frac{\rho_{ij+1}-\rho_{ij}}{\Delta y}L_{ij+\frac{1}{2}} - \frac{\rho_{ij}-\rho_{ij-1}}{\Delta y}L_{ij-\frac{1}{2}}, \tag{9}$$

where $L_{i\pm1/2}$ (resp. $L_{j\pm1/2}$) refers to the length of the face in Ω^- between i and $i\pm1$ (resp. j and $j\pm1$) as depicted in Fig. 1 (right).

We then apply the Robin boundary condition (5) to each cell that contains a portion of Γ by substituting the value of $\nabla\rho\cdot\mathbf{n}$ from the boundary condition into the second term of the right hand side of (8),

$$\int_{\mathcal{C}_{ij}\cap\Gamma} \nabla\rho\cdot\mathbf{n}\,dl = \int_{\mathcal{C}_{ij}\cap\Gamma} (f-\alpha\rho)\,dl. \tag{10}$$

Here, we also use the approximation of constant ρ within the cell, but we must evaluate the integral containing f carefully since this term is only valid on Γ, not throughout the entire cell,

$$\int_{\mathcal{C}_{ij}\cap\Gamma} (f-\alpha\rho)\,dl = -\alpha\rho_{ij}L_{\mathcal{C}_{ij}\cap\Gamma} + \int_{\mathcal{C}_{ij}\cap\Gamma} f\,dl. \tag{11}$$

In this work, we leverage the recent work of Min and Gibou [19,20] in the discretization of the Dirac delta functions. A hallmark of this approach is that it is robust to perturbations of the interface on the grid. We next discuss the procedure we use for calculating line and area integrals in Section 3.2. We note that this approach is a generalization of solving the Poisson equation with homogeneous Neumann boundary condition that one encounters in typical projection methods for fluid flows [23].

3.2. Calculating line and area integrals

For the sake of clarity, we will briefly describe the geometric approach of [19,20] for calculating line and surface integrals over an irregular domain, Ω^-. This approach utilizes an implicit function to represent the irregular domain and produces second-order accurate results which are independent of the interface location on the grid.

The general procedure is to decompose grid cells into a union of triangles and approximate $S\cap\Gamma$ (Fig. 2) and $S\cap\Omega^-$ (Fig. 3), with a linear interpolation of ϕ, stored at the vertices of each triangle. With this approach, the line and area integrals can be calculated as the sum of the integrals over each simplex, S,

$$\int_\Gamma f\,d\Gamma = \sum_{\mathcal{C}:\text{grid cell}} \int_{\mathcal{C}\cap\Gamma} f\,d\Gamma = \sum_{\mathcal{C}:\text{grid cell}} \sum_{S\in T(\mathcal{C})} \int_{S\cap\Gamma} f\,d\Gamma,$$
$$\int_{\Omega^-} f\,d\Omega = \sum_{\mathcal{C}:\text{grid cell}} \int_{\mathcal{C}\cap\Omega^-} f\,d\Omega = \sum_{\mathcal{C}:\text{grid cell}} \sum_{S\in T(\mathcal{C})} \int_{S\cap\Omega^-} f\,d\Omega,$$

where $T(\mathcal{C})$ is the triangulation of a cell $\mathcal{C}$, i.e., $\mathcal{C}=\bigcup_{S\in T(\mathcal{C})}S$ and where the second-order midpoint method is used to calculate the integrals. We refer the interested reader to [19] for more details of the integration procedure.

3.2.1. Properties of the linear system

The linear system is symmetric and positive definite. Indeed for a cell in Ω^- with neighbors also in Ω^-, the discretization leads to the usual symmetric discretization of the Crank–Nicholson scheme. For cells cut by the interface this property is

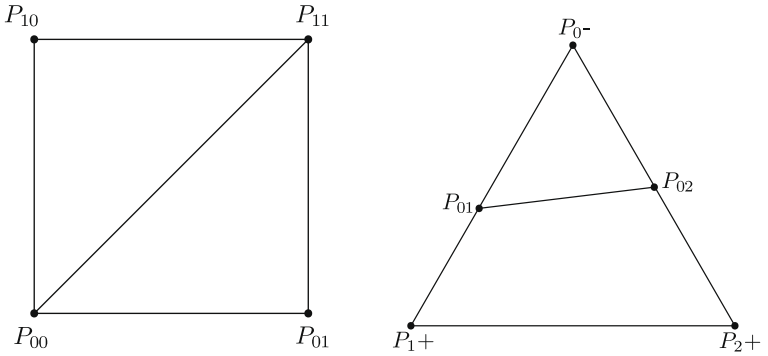

Fig. 2. Triangulation of a cell (left), and the general representations of $S\cap\Gamma$ (right).

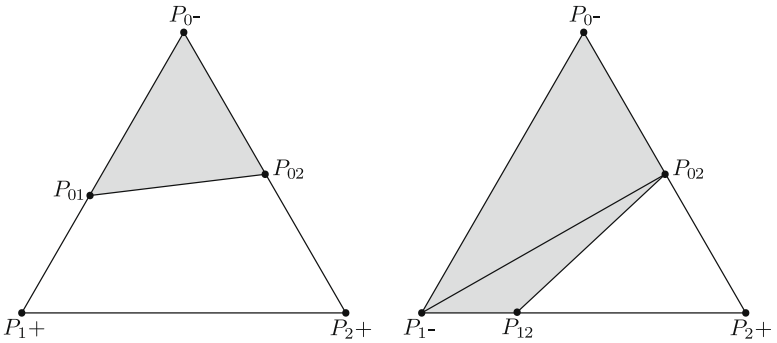

Fig. 3. The two general representations of $S \cap \Omega^-$.

retained and is illustrated geometrically in Fig. 1 (right). Consider the coefficient of $\rho_{i-1,j}$, which comes from the discretization in cell $\mathcal{C}_{ij}$, and the coefficient of ρ_{ij}, which comes from the discretization in cell $\mathcal{C}_{i-1,j}$. We have:

$$A_{i-1,j}^{\mathcal{C}_{ij}} = \frac{k\Delta t}{2\Delta x} L_{i-\frac{1}{2}j}^{\mathcal{C}_{ij}} \quad \text{and} \quad A_{ij}^{\mathcal{C}_{i-1,j}} = \frac{k\Delta t}{2\Delta x} L_{i+\frac{1}{2}j}^{\mathcal{C}_{i-1,j}}. \tag{12}$$

Since $L_{i-\frac{1}{2}j}^{\mathcal{C}_{ij}} = L_{i+\frac{1}{2}j}^{\mathcal{C}_{i-1,j}}$, the two coefficients are equal, consequently the matrix is symmetric. We note that the terms that arise from the boundary, Γ, do not affect the symmetry of the linear system since they appear only in the diagonal coefficient and in the right hand side.

The discretization results in strictly positive diagonal elements and a diagonally dominant linear system for problems that are formulated with a positive value of α in the boundary condition (5), therefore, the linear system is positive definite.

In conclusion, the linear system is symmetric and positive definite. Accordingly, fast linear solvers can be used to invert it. In the example section, we use the conjugate gradient method with an incomplete Cholesky preconditioner.

4. Numerical approach for Stefan-type problems with Robin boundary condition

Here we consider the Stefan problem, where ρ is determined by the diffusion equation (4) with a Robin boundary condition (5) on the moving interface Γ. The interface velocity is determined by

$$\mathbf{V} = D[\nabla\rho]_\Gamma, \tag{13}$$

where D is a velocity coefficient and $[\cdot]$ denotes a jump in the gradient of ρ across the interface. The level set function, ϕ, implicitly defines and captures the evolution of the interface according to the advection equation

$$\phi_t + D[\nabla\rho] \cdot \nabla\phi = 0.$$

4.1. Algorithm

We use the following algorithm to solve the Stefan problem: Given the solution ρ^n at time t^n,

1. Extrapolate the initial field, ρ^n, outward from the interface to cover a few grid cells in order to define valid values that will be used when assembling the right hand side of the linear system at time t^{n+1} (see Section 4.1.1).
2. Calculate the velocity field, $\mathbf{V}$, from the gradient of ρ^n.
3. Advect ϕ^n to obtain the new boundary location, ϕ^{n+1}.
4. Assemble the linear system and right hand side on the irregular domain described by ϕ^{n+1}.
5. Solve the diffusion equation to find the new field, ρ^{n+1}.
6. Repeat from Step 1.

We describe each step in what follows:

4.1.1. Extrapolation of ρ values

In the case of an advancing interface, when assembling the linear system for time t^{n+1}, the values of ρ at time t^n will be needed at grid locations which were outside of the interface at t^n but are swept by the interface from t^n to t^{n+1}. In order to define these ghost cell values, we use quadratic extrapolation in the normal direction to the t^n interface as described in [1]:

The extrapolation is done in a series of steps. First, the second directional derivative of ρ in the normal direction is defined only in the interior region Ω^-,

$$\rho_{nn} = \mathbf{n} \cdot \nabla(\mathbf{n} \cdot \nabla\rho). \tag{14}$$

Next, this scalar function is extrapolated in a constant manner over the interface by solving for a few time steps:

$$\frac{\partial \rho_{nn}}{\partial \tau} + H(\phi^n)\mathbf{n} \cdot \nabla\rho_{nn} = 0, \tag{15}$$

where $H(\phi^n)$ is the Heaviside function which is used to not disturb the known values of ρ_{nn} in the region $\phi \leqslant 0$. Once the second directional derivative is defined over a band around the interface, we can solve for the first directional derivative, ρ_n, by solving the PDE,

$$\frac{\partial \rho_n}{\partial \tau} + H(\phi^n)(\mathbf{n} \cdot \nabla\rho_n - \rho_{nn}) = 0, \tag{16}$$

which defines ρ_n to have a directional derivative equal to ρ_{nn}. Finally, we solve a similar equation which defines the values of ρ to have a directional derivative equal to ρ_n,

$$\frac{\partial \rho}{\partial \tau} + H(\phi^n)(\mathbf{n} \cdot \nabla\rho - \rho_n) = 0. \tag{17}$$

These PDEs are solved over a fictitious time τ, and it is only necessary to iterate a few time steps to obtain extrapolated values of ρ in a narrow band around the interface.

4.1.2. Calculating the velocity field

The velocity of the advancing interface is calculated according to Eq. (13). For our simple Stefan problem, we have assumed that ρ is constant within Ω^+, therefore, the velocity is determined solely by the gradient within Ω^-. In the case where the solution is to be computed on both Ω^- and Ω^+, thus the velocity computed by the jump across the interface, the velocity is computed node-by-node after extrapolating the solution on Ω^- to Ω^+ and the solution on Ω^+ to Ω^-. Of course, two copies of the original solution are stored before taking this step. The interested reader is referred to [10,11] for more details.

Once the gradient of ρ is defined, the velocity field is calculated in two steps. The first step is to calculate the velocity in a node-by-node basis according to Eq. (13). We then use constant extrapolation in the normal direction first outward from the interface toward Ω^+, and then inward from Γ toward Ω^- in order to define the velocity field in a band around the interface.

4.1.3. Advancing the interface

We keep track of the interface evolution in time by solving the advection Eq. (1). Here we use a second-order-accurate Semi-Lagrangian method as described in [37]. This method is implicit and unconditionally stable, so that large time steps may be used. Semi-Lagrangian methods reconstruct the solution by integrating numerically along characteristic curves starting from any grid point, x_i, and tracing back the departure point, x_d, in the upwind direction. Interpolating formulas are used to recover the value of the solution.

More precisely, the solution at a grid point, x_i is found by

$$\phi^{n+1}(x_i) = \phi^n(x_d), \tag{18}$$

where x_d is the corresponding departure point. We use a second order explicit midpoint method to integrate numerically,

$$\hat{x} = x^{n+1} - \frac{\Delta t}{2} \cdot V^n(x^{n+1}), \tag{19}$$

$$x_d^n = x^{n+1} - \Delta t \cdot V^{n+1/2}(\hat{x}), \tag{20}$$

$$V^{n+1/2} = \frac{3}{2}V^n - \frac{1}{2}V^{n-1}. \tag{21}$$

The values of $\hat{x}$ and $\phi^n(x_d^n)$ may not be located on a grid node, therefore, they can be approximated by interpolation schemes (piecewise bilinear in our case).

5. Examples

5.1. Poisson solution over a circular domain

Consider a solution to the Poisson equation $\Delta\rho = f$ over a circular domain. The problem is formulated with a Robin boundary condition (5) with $\alpha = 1$. The interior region, Ω^- is described by a circle of radius $r = 0.75$ centered at the origin and the computational domain is taken as $[-1,1] \times [-1,1]$. The simulation was compared against the exact solution of $\rho = e^{xy}$. Fig. 4 depicts the numerical solution. The solution is second-order accurate in the L^1 and L^∞ norms as demonstrated in Fig. 5.

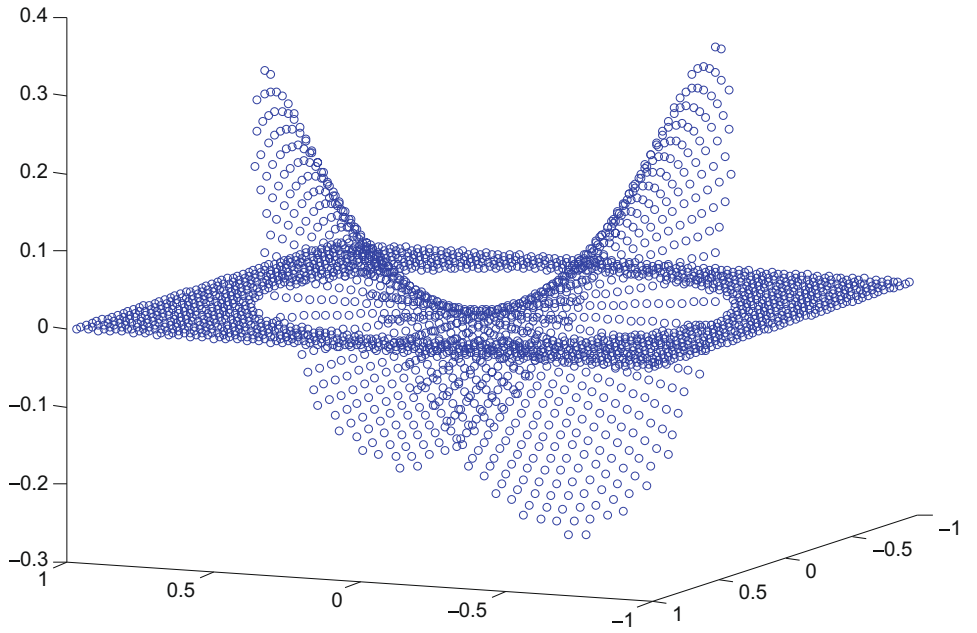

Fig. 4. Solution to the Poisson equation over the circle domain (Example 5.1).

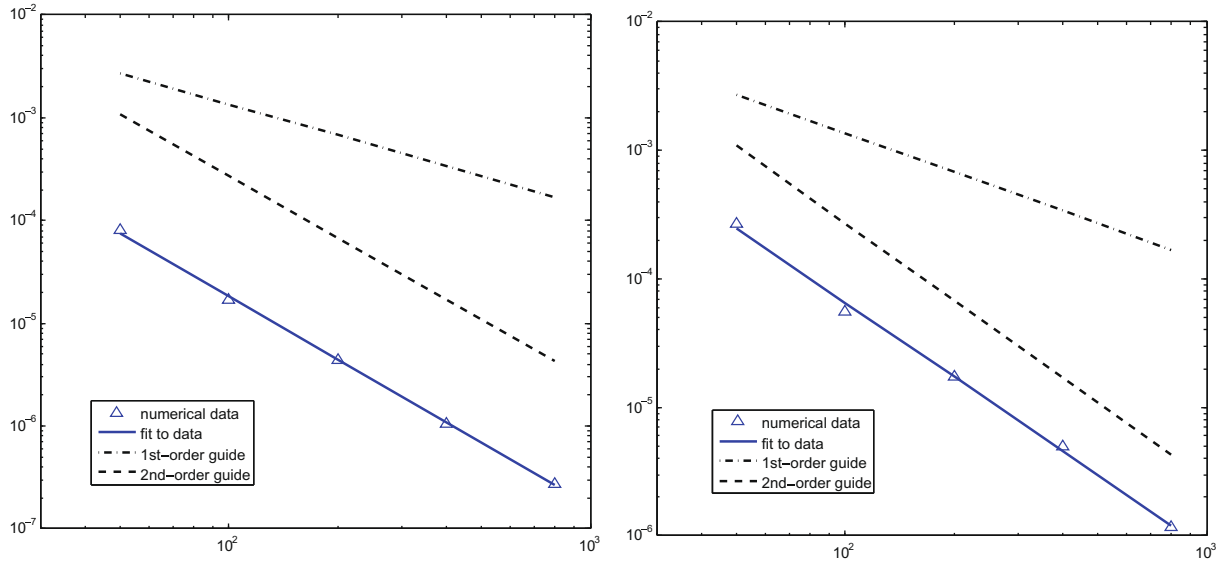

Fig. 5. Error analysis in the L^1 norm (left) and L^∞ norm (right) of the Poisson solution over the circular domain (Example 5.1). The triangle markers are the numerical data. The solid lines are least-squares fits to the data with slopes -2.04 and -1.92. The dashed lines are first and second-order visual guides.

5.2. Poisson solution over a flower-shaped domain

Consider a solution to the Poisson equation $\Delta\rho = f$ over a flower-shaped domain. The boundary of the five-petal flower is defined by the zero level set of $\phi = r - 0.5 - \frac{y^5+5x^4y-10x^2y^3}{3r^5}$. The computational domain is taken as $[-1,1]\times[-1,1]$. A Robin boundary condition (5) with $\alpha = 1$ is used to formulate the problem. We compare our simulation against the exact solution

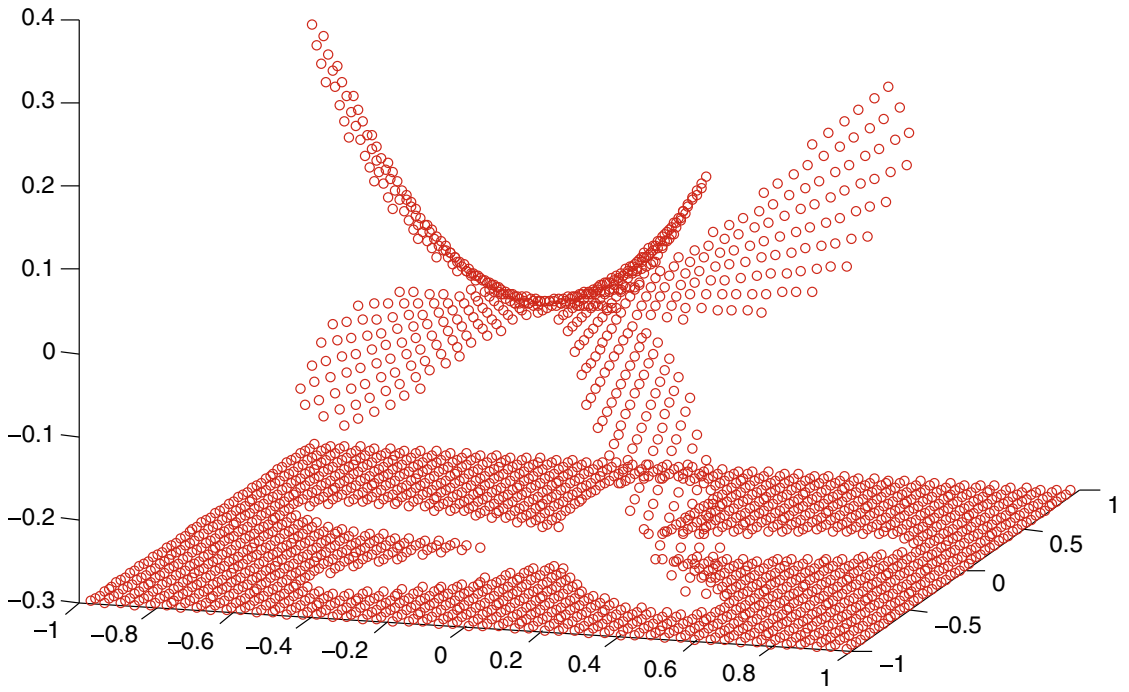

Fig. 6. Solution to the Poisson equation over the flower domain (Example 5.2).

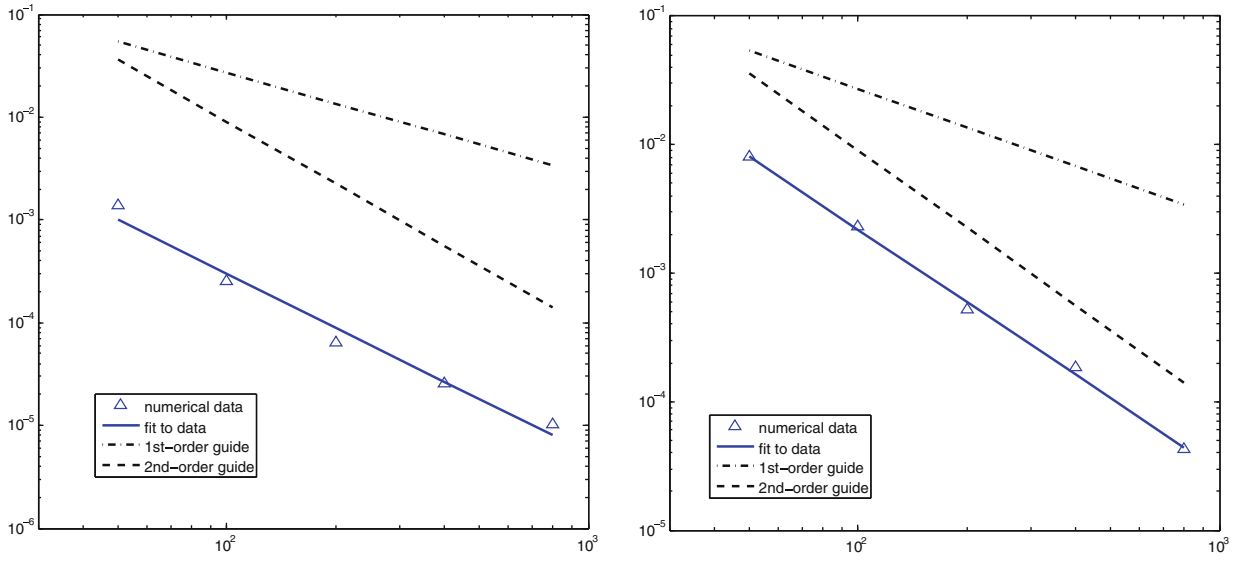

Fig. 7. Error analysis in the L^1 norm (left) and L^∞ norm (right) of the Poisson solution over the flower domain (Example 5.2). The triangle markers are the numerical data. The solid lines are least-squares fits to the data with slopes -1.74 and -1.88. The dashed lines are first and second-order visual guides.

of $\rho = e^{xy}$. A plot of the numerical solution is displayed in Fig. 6. The accuracy results are presented in Fig. 7. The solution is approximately second-order accurate in the L^1 and L^∞ norms.

5.3. Heat solution over a circular domain

We present a solution to the heat equation (4) with $k = 1$ over a circular domain of radius $r = \pi$, centered at the origin. The computational domain is $[-1.5\pi, 1.5\pi] \times [-1.5\pi, 1.5\pi]$. The Robin boundary condition (5) is formulated with $\alpha = 1$. We

compare our numerical solution against the exact solution of $\rho = -e^{-2t}\cos(x)\cos(y)$. The simulation was run from time $t = 0$ to $t = 0.5$ with a time step of $dt = dx$. The accuracy results of the solution are presented in Fig. 8. As with the Poisson examples, the solution is second-order accurate in the L^1 and L^∞ norms.

5.4. Heat solution over a flower-shaped domain

Consider a solution to the heat equation (4) with $k = 1$ over a five-petal flower shape. The problem is formulated with a Robin boundary condition (5) with $\alpha = 1$. The boundary of the flower is defined by the zero level set of $\phi = r - 0.5 - \frac{y^5+5x^4y-10x^2y^3}{3r^5}$, and the computational domain is taken as $[-1,1]\times[-1,1]$. The exact solution has the form $\rho = -e^{-2t}\cos(x)\cos(y)$. A plot of the numerical solution at three time steps is displayed in Fig. 9. The accuracy results are presented in Fig. 10. The solution is second-order accurate in the L^1 and L^∞ norms.

5.5. Examples for the Stefan problem

5.5.1. 2D Frank sphere solution with Robin boundary condition

The Frank sphere solution [9] that describes the growing solidification of a cylinder in 2D was reformulated with a Robin boundary condition. We begin with the radial heat equation expressed with a similarity variable, $s = rt^{-\frac{1}{2}}$,

$$\frac{\partial^2 T}{\partial s^2} = -\left(\frac{s}{2}+\frac{1}{s}\right)\frac{\partial T}{\partial s},$$

where T is the temperature. We can integrate once with a change of variable,

$$\frac{\partial T}{\partial s} = As^{-1}e^{-\frac{s^2}{4}}.$$

Integrating, we obtain an expression for T,

$$T = A\int_\infty^s z^{-1}e^{-\frac{z^2}{4}}dz + B,$$

which can also be written using the error function E_1,

$$T = -\frac{A}{2}\mathrm{E}_1\left(\frac{s^2}{4}\right) + B. \tag{22}$$

The far-field boundary condition may be applied to Eq. (22) to set the integration constant $B = T_\infty$. The second integration constant, A, is found by recognizing that the temperature must remain continuous at the interface. Since $T = 0$ in the solid phase (Ω^+), then $T = 0$ on the interface. Furthermore, A is constrained by the initial radius, R_o, and time, t_o,

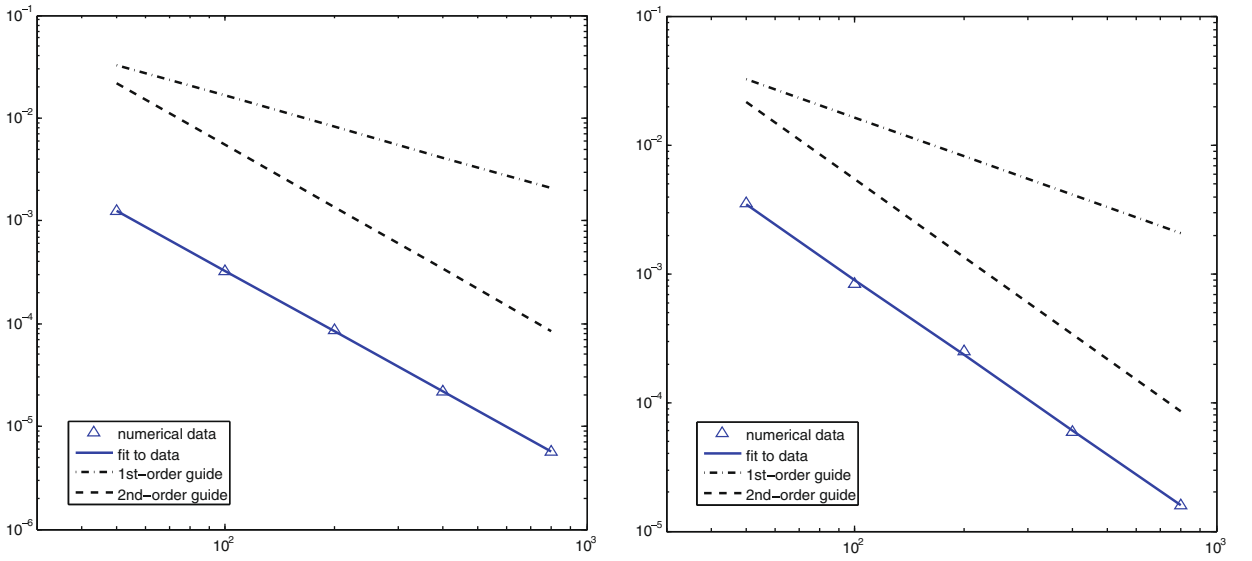

Fig. 8. Error analysis in the L^1 norm (left) and L^∞ norm (right) of the heat solution over the circle domain (Example 5.3). The triangle markers are the numerical data. The solid lines are least-squares fits to the data with slopes −1.95 and −1.95. The dashed lines are first and second-order visual guides.

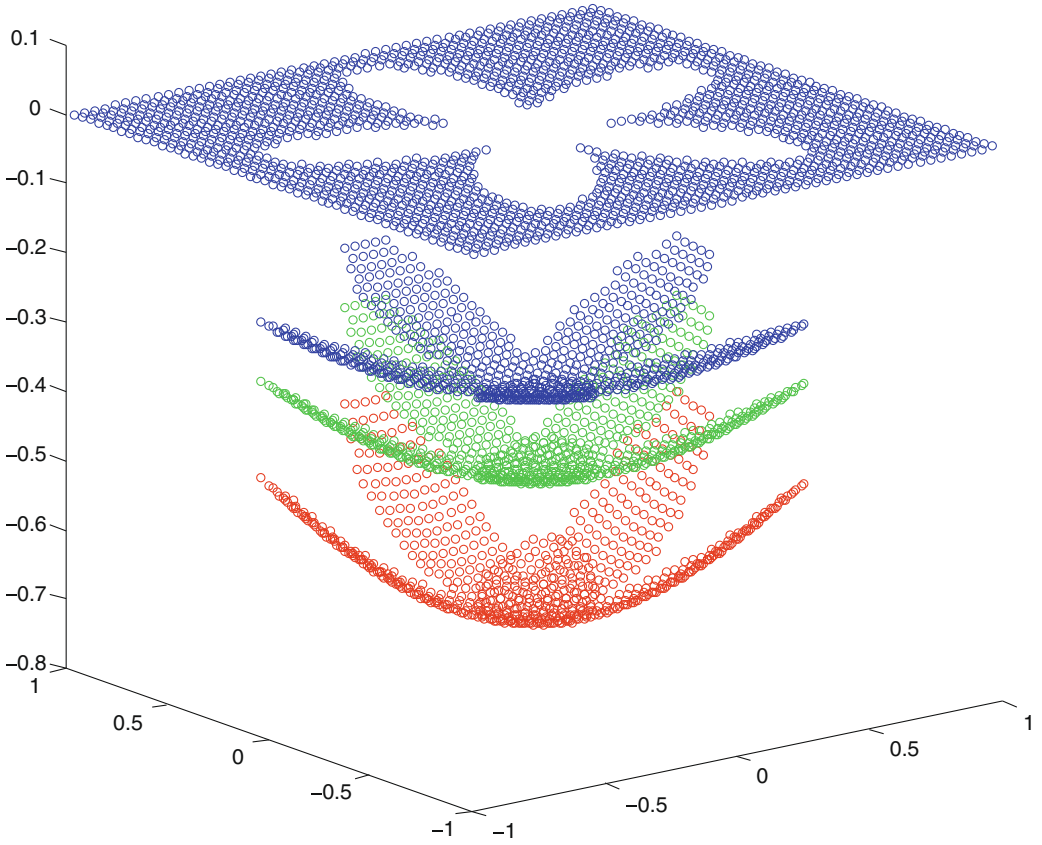

Fig. 9. Solution to the heat equation over the flower domain (5.4). The solution is shown in red at $t = 0$, in green at $t = 0.35$, and blue at $t = 0.5$. (For interpretation of the references to colour in this figure legend, the reader is referred to the web version of this article.)

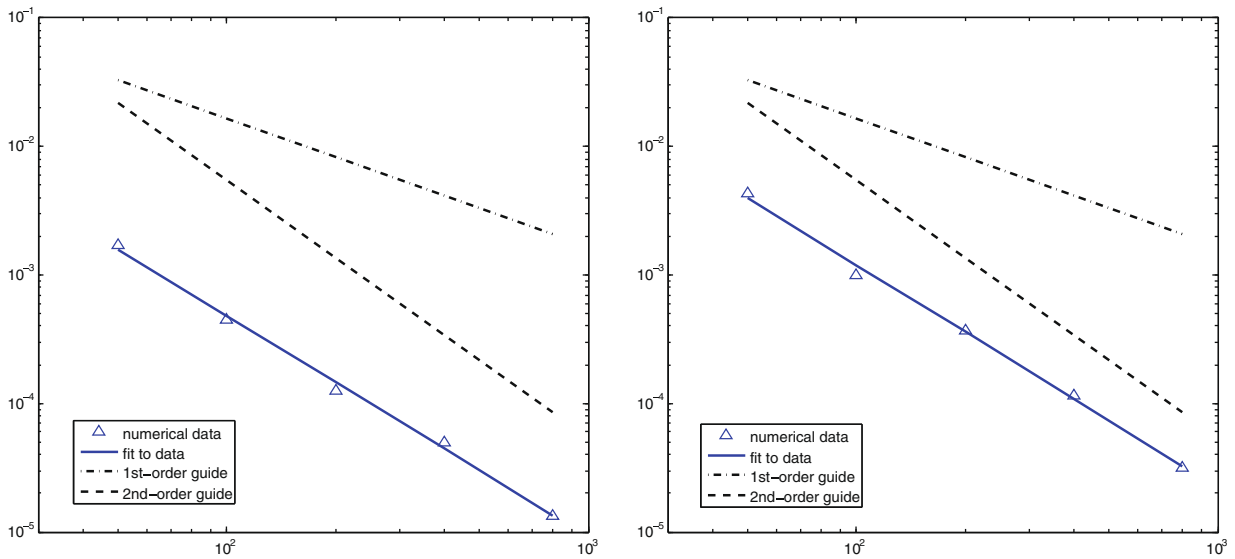

Fig. 10. Error analysis in the L^1 norm (left) and L^∞ norm (right) of the heat solution over the flower domain (5.4). The triangle markers are the numerical data. The solid lines are least-squares fits to the data with slopes -1.72 and -1.73. The dashed lines are first and second-order visual guides.

$$S_o = s(R_o, t_o) = R_o t_o^{-\frac{1}{2}},$$
$$A = \frac{2T_\infty}{\mathrm{E}_1\left(\frac{S_o^2}{4}\right)}.$$

After applying the expressions for both integration constants to Eq. (22), the temperature profile in Ω^- takes the form,

$$T = T_\infty \left(1 - \frac{\mathrm{E}_1\left(\frac{s^2}{4}\right)}{\mathrm{E}_1\left(\frac{S_o^2}{4}\right)}\right). \tag{23}$$

In the case of a Robin boundary condition (5) and radial symmetry, we have

$$\nabla T \cdot \mathbf{n} = \frac{\partial T}{\partial r} = \frac{\partial T}{\partial s}\frac{\partial s}{\partial r} = \frac{2T_\infty}{\mathrm{E}_1\left(\frac{S_o^2}{4}\right)} t^{-\frac{1}{2}} s^{-1} e^{-\frac{s^2}{4}},$$

and

$$f(s,t) = \frac{2T_\infty}{\mathrm{E}_1\left(\frac{S_o^2}{4}\right)} t^{-\frac{1}{2}} s^{-1} e^{-\frac{s^2}{4}} + \alpha T_\infty \left(1 - \frac{\mathrm{E}_1\left(\frac{s^2}{4}\right)}{\mathrm{E}_1\left(\frac{S_o^2}{4}\right)}\right). \tag{24}$$

The initial front velocity, V_n, is given by:

$$V_{n|_{\Gamma_o}} = -[\nabla T \cdot \mathbf{n}]_{|_{\Gamma_o}} = -\frac{2T_\infty}{\mathrm{E}_1\left(\frac{S_o^2}{4}\right)} t_o^{-\frac{1}{2}} S_o^{-1} e^{-\frac{S_o^2}{4}}. \tag{25}$$

Also, since the interface remains a cylinder as it grows in time, $R(t) = S_o t^{\frac{1}{2}}$,

$$V_{n|_\Gamma} = \frac{dR}{dt} = \frac{S_o}{2t^{\frac{1}{2}}}. \tag{26}$$

By combining Eqs. (25) and (26), we obtain the relationship between T_∞ and S_o,

$$T_\infty = -\frac{S_o^2}{4}\mathrm{E}_1\left(\frac{S_o^2}{4}\right) e^{-\frac{S_o^2}{4}}. \tag{27}$$

Consider a simulation over the domain $[-3,3]\times[-3,3]$. The far-field temperature is chosen to be $T_\infty = -0.25$, thus giving an initial radius of $R_o = 0.75$. The problem is formulated with $\alpha = 1$ in the boundary condition (5) and (24). The simulation is run from time $t = 1$ to $t = 2$.

The accuracy of the temperature field and the radius location are presented in Figs. 11 and 12, respectively. A measurement of the radius location is linearly interpolated from every grid interval in which the level set function changes sign. Both the temperature and the radius are first-order accurate. This is consistent with our expectations of the method since the solution depends on the gradient of the temperature field.

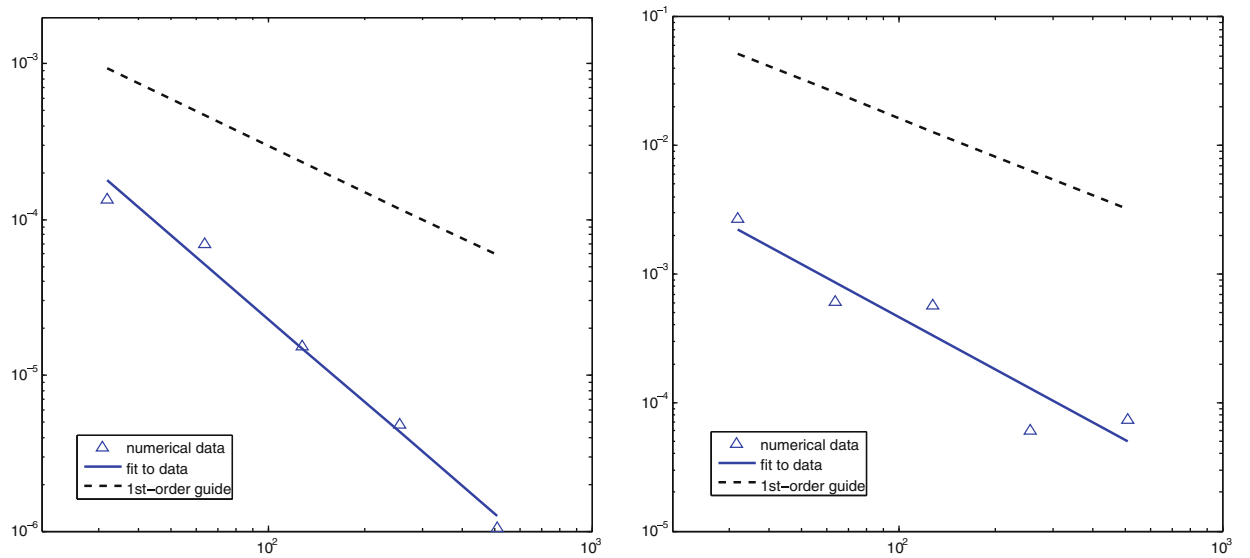

Fig. 11. Error analysis in the L^1 norm (left) and L^∞ norm (right) of the temperature of the Frank sphere solution (Example 5.5.1). The triangle markers are the numerical data. The solid lines are least-squares fits to the data with slopes −1.79 and −1.37. The dashed lines are 1st-order visual guides.

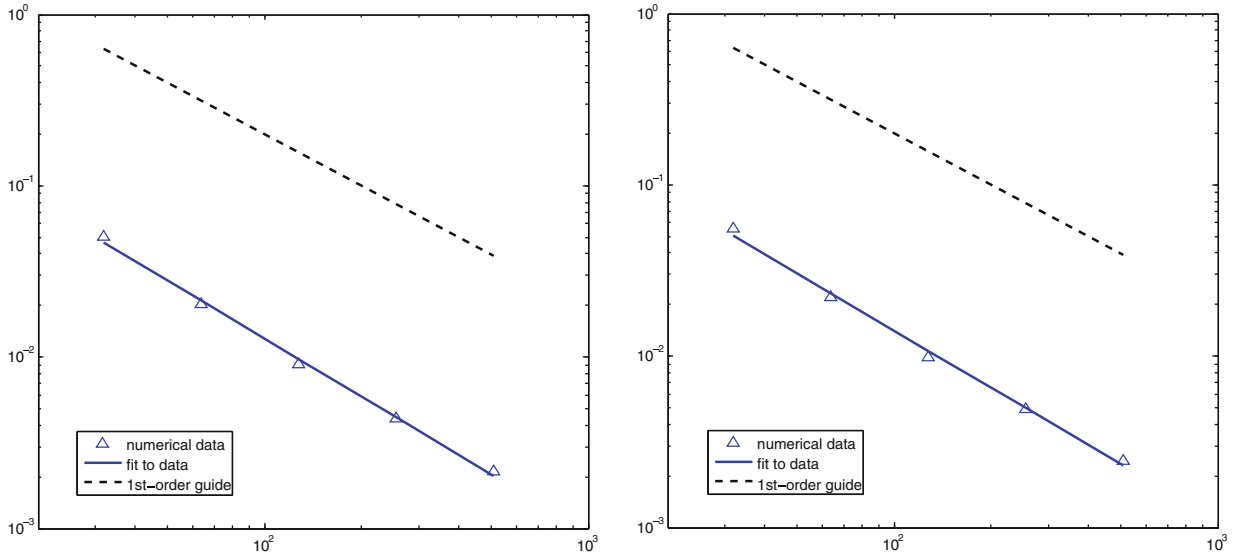

Fig. 12. Error analysis in the L^1 norm (left) and L^∞ norm (right) of the radius of the Frank sphere solution (Example 5.5.1). The triangle markers are the numerical data. The solid lines are least-squares fits to the data with slopes -1.13 and -1.17. The dashed lines are 1st-order visual guides.

5.5.2. 2D frank sphere with Robin boundary condition and discontinuous solution

We present an exact solution to the Stefan problem with a discontinuous solution across the interface. The solution is formulated from the above Frank sphere solution. The temperature profile takes the form,

$$T = 0, \quad \mathbf{x} \in \Omega^+$$
$$T = T_\infty - (T_\infty + 0.1)\frac{E_1\left(\frac{s^2}{4}\right)}{E_1\left(\frac{s_0^2}{4}\right)}, \quad \mathbf{x} \in \Omega^-. \tag{28}$$

This solution describes a cylinder growing radially outward. The temperature inside the cylinder is zero and the temperature profile has a jump at the interface $\Delta T = -0.1$. The boundary condition is given by (5) with $\alpha = 1$. The velocity of the moving boundary is given by

$$V_n = -D\nabla\rho \cdot \mathbf{n}, \tag{29}$$

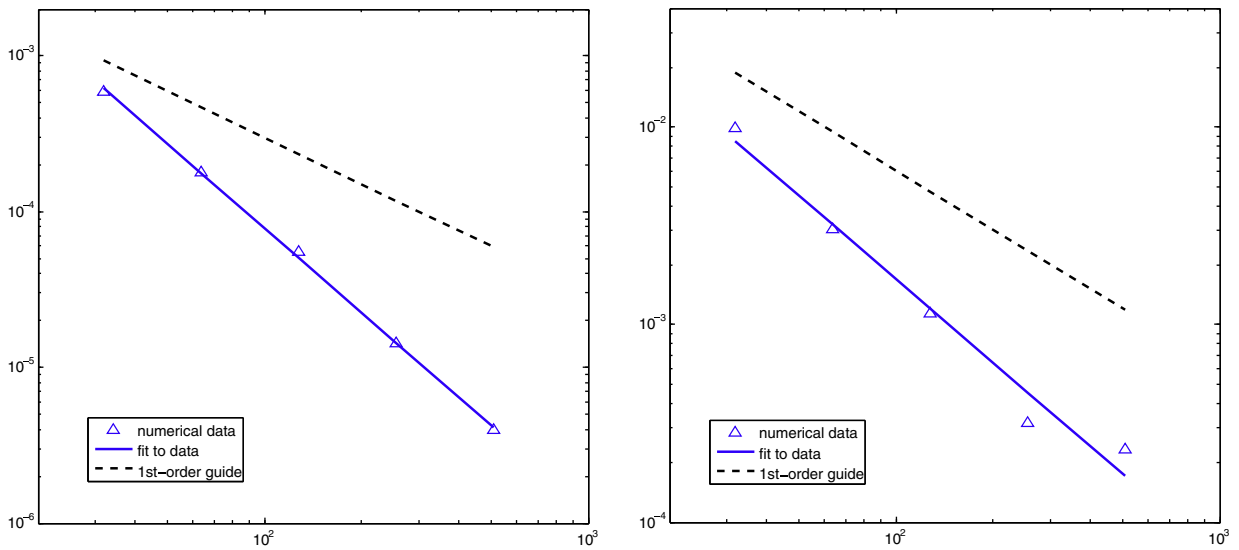

Fig. 13. Error analysis in the L^1 norm (left) and L^∞ norm (right) of the temperature of the discontinuous Frank sphere solution (Example 5.5.1). The triangle markers are the numerical data. The solid lines are least-squares fits to the data with slopes -1.81 and -1.41. The dashed lines are 1st-order visual guides.

where the velocity coefficient, D, is given by

$$D = \frac{S_0 s}{4(T_\infty + 0.1)} e^{\frac{s^2}{4}} E_1\left(\frac{S_0^2}{4}\right), \tag{30}$$

and constrains the growth of the cylinder such that the radius evolves by $R = S_0 t^{\frac{1}{2}}$.

With a chosen temperature value of $T_\infty = -0.5$, the initial sphere radius is $R = 1.56$. The simulation is computed over the time $t = 1$ to $t = 2.5$. The results are presented in Figs. 13 and 14. The temperature profile and the radius location are first-order accurate.

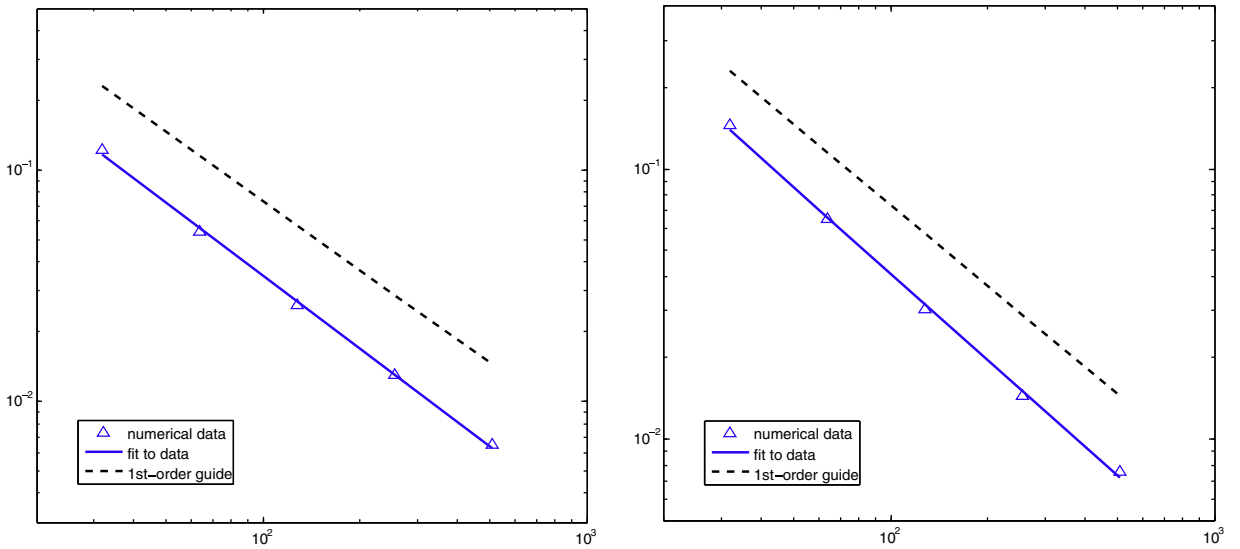

Fig. 14. Error analysis in the L^1 norm (left) and L^∞ norm (right) of the radius of the discontinuous Frank sphere solution (Example 5.5.2). The triangle markers are the numerical data. The solid lines are least-squares fits to the data with slopes -1.05 and -1.07. The dashed lines are 1st-order visual guides.

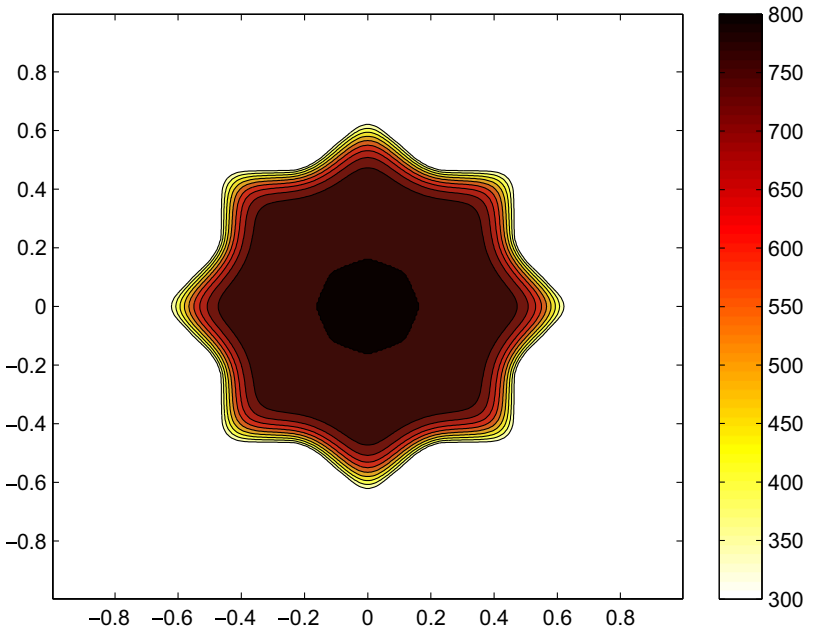

Fig. 15. Temperature contour plot after 30 s of cooling for Example 5.5.3.

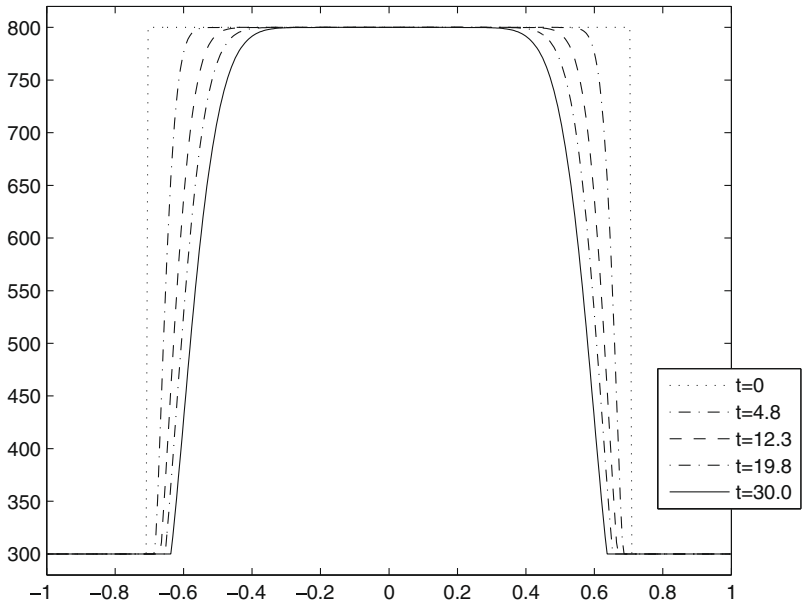

Fig. 16. Temperature evolution of Example 5.5.3.

5.5.3. Heat transfer in a convectively cooled body

We provide an example of a classical heat transfer problem involving conduction within a solid body and convection at the object's boundary. In contrast to the previous examples, this problem does not have an analytical solution for comparison. A backward Euler time discretization was used in conjunction with our approach for the Laplacian outlined in Section 3.1.

Consider a two-dimensional solid body, initially at temperature, $T = 1300\,\mathrm{K}$ and with the initial shape of a $\{8/2\}$ star polygon with tip-to-tip length of $\sqrt{2}$. The temperature of the object is found by solving the heat equation,

$$\rho C_p T_t = k\Delta T. \tag{31}$$

Balancing heat conduction and convection at the interface gives the following Robin boundary condition,

$$-k\nabla T \cdot \mathbf{n} = h(T - T_\infty). \tag{32}$$

In this example we consider the material properties of copper: density, $\rho = 8,954\,\mathrm{kg/m^3}$, heat capacity at constant pressure, $C_p = 384\,\mathrm{J/kg\,K}$, and thermal conduction coefficient, $k = 378\,\mathrm{W/m\,K}$. With a chosen value of the convection coefficient, $h = 3072\,\mathrm{W/m^2\,K}$, the corresponding Biot number is $Bi = 2$, therefore, internal conduction and convection are both relevant to the solution. The ambient temperature is taken as $T_\infty = 300\,\mathrm{K}$. We used a simple model for simulating thermal expansion, in which the boundary normal velocity is set to a constant value of -0.001.

Fig. 15 is a contour plot of the temperature distribution after a cooling period of 30 s. Fig. 16 shows the temperature evolution of the $y = 0$ cross-section.

6. Conclusions

We have proposed a straightforward and efficient method for the solution of the Poisson, heat, and Stefan-type problems with Robin boundary conditions over possibly moving, arbitrarily-shaped domains. Our approach utilizes the level set framework so that complex interface topology is implicitly captured. This is straightforward to implement with a cell-based discretization of the domain and a geometric based method [19] for calculating the resulting integrals. The approach produces symmetric and positive definite linear systems so that fast iterative solvers may be used. We have shown this method to be second-order accurate for the Poisson and heat equations, and first-order accurate for Stefan-type problems. This approach can be easily adapted to more advanced applications and models where the requisite physics involve Robin boundary conditions.

Acknowledgments

The research of J. Papac and F. Gibou was supported in part by a Sloan Research Fellowship in Mathematics, by the National Science Foundation under Grant Agreement DMS 0713858, by the Institute for Collaborative Biotechnologies through

contract no. W911NF-09-D-0001 from the U.S. Army Research Office, and by the Department of Energy under Grant Agreement DE-FG02-08ER15991. FG acknowledges helpful discussion with Prof. Chohong Min.

References

[1] T. Aslam, A partial differential equation approach to multidimensional extrapolation, J. Comput. Phys. 193 (2004) 349–355.
[2] K. Brattkus, D.I. Meiron, Numerical simulations of unsteady crystal growth, SIAM J. Appl. Math. 52 (1992) 1303.
[3] R. Caflisch, M. Gyure, B. Merriman, S. Osher, C. Ratsch, D. Vvedensky, J. Zinck, Island dynamics and the level set method for epitaxial growth, Appl. Math. Lett. 12 (1999) 13.
[4] R. Caiden, R. Fedkiw, C. Anderson, A numerical method for two phase flow consisting of separate compressible and incompressible regions, J. Comput. Phys. 166 (2001) 1–27.
[5] S. Chen, B. Merriman, S. Osher, P. Smereka, A simple level set method for solving Stefan problems, J. Comput. Phys. 135 (1997) 8–29.
[6] G. Ehrlich, F.G. Hudda, Atomic view of surface self-diffusion: Tungsten on tungsten, J. Chem. Phys. 44 (1966) 1039.
[7] R. Fedkiw, T. Aslam, B. Merriman, S. Osher, A non-oscillatory Eulerian approach to interfaces in multimaterial flows (the ghost fluid method), J. Comput. Phys. 152 (1999) 457–492.
[8] R. Fedkiw, T. Aslam, S. Xu, The ghost fluid method for deflagration and detonation discontinuities, J. Comput. Phys. 154 (1999) 393–427.
[9] F. Frank, Proc. R. Soc. A 201 (1950) 586.
[10] F. Gibou, R. Fedkiw, R. Caflisch, S. Osher, A level set approach for the numerical simulation of dendritic growth, J. Sci. Comput. 19 (2003) 183–199.
[11] F. Gibou, R. Fedkiw, L.-T. Cheng, M. Kang, A second-order-accurate symmetric discretization of the Poisson equation on irregular domains, J. Comput. Phys. 176 (2002) 205–227.
[12] F. Gibou, R. Fedkiw, A fourth order accurate discretization for the laplace and heat equations on arbitrary domains with applications to the Stefan problem, J. Comput. Phys. 202 (2005) 577–601.
[13] F. Gibou, C. Ratsch, R. Caflisch, Capture numbers in rate equations and scaling laws for epitaxial growth, Phys. Rev. B 67 (2003) 155403.
[14] F. Gibou, C. Ratsch, S. Chen, M. Gyure, R. Caflischm, Rate equations and capture numbers with implicit island correlations, Phys. Rev. B 63 (2001) 115401.
[15] A. Karma, W.-J. Rappel, Phase-field modeling method for computationally efficient modeling of solidification with arbitrary interface kinetics, Phys. Rev. E 53 (1996).
[16] A. Karma, W.-J. Rappel, Quantitative phase-field modeling of dendritic growth in two and three dimensions, Phys. Rev. E 57 (1997) 4323–4349.
[17] A. Karma, Phase-field formulation for quantitative modeling of alloy solidification, Phys. Rev. Lett. 87 (2001) 115701.
[18] J.S. Langer, in: G. Grinstein, G. Mazenko (Eds.), Directions in Condensed Matter Physics, World Scientific, Singapore, 1986.
[19] C. Min, F. Gibou, Geometric integration over irregular domains with application to level set methods, J. Comput. Phys. 226 (2007) 1432–1443.
[20] C. Min, F. Gibou, Robust second order accurate discretization of the multi-dimensional Heaviside and Dirac delta functions, J. Comput. Phys. 227 (2008) 9686–9695.
[21] B. Nestler, D. Danilov, P. Galenko, Crystal growth of pure substances: phase-field simulations in comparison with analytical and experimental results, J. Comput. Phys. 207 (2005) 221–239.
[22] D. Nguyen, R. Fedkiw, M. Kang, A boundary condition capturing method for incompressible flame discontinuities, J. Comput. Phys. 172 (2001) 71–98.
[23] Y.T. Ng, C. Min, F. Gibou, Efficient fluid-solid coupling for one phase flows, J. Comput. Phys. 228 (2009) 8807–8829.
[24] R.H. Nochetto, M. Paolini, C. Verdi, An adaptive finite element method for two-phase Stefan problems in two space dimensions. Part II: Implementation and numerical experiments, SIAM J. Sci. Stat. Comput. 12 (1991) 1207.
[25] S. Osher, R. Fedkiw, Level Set Methods and Dynamic Implicit Surfaces, Springer-Verlag, New York, NY, 2002.
[26] S. Osher, N. Paragios, Geometric Level Set Methods in Imaging Vision and Graphics, Springer-Verlag, New York, NY, 2003.
[27] S. Osher, J. Sethian, Fronts propagating with curvature-dependent speed: algorithms based on Hamilton–Jacobi formulations, J. Comput. Phys. 79 (1988) 12–49.
[28] C. Ratsch, M. Gyure, F. Gibou, M. Petersen, M. Kang, J. Garcia, D. Vvedensky, Level-set method for island dynamics in epitaxial growth, Phys. Rev. B 65 (2002) 195403.
[29] Y. Saad, Iterative Methods for Sparse Linear Systems, PWS Publishing, New York, NY, 1996.
[30] A. Schmidt, Computation of three dimensional dendrites with finite elements, J. Comput. Phys. 125 (1996) 293–312.
[31] R.L. Schwoebel, E.J. Shipsey, Step motion on crystal surfaces, J. Appl. Phys. 37 (1966) 3682.
[32] J.A. Sethian, Level Set Methods and Fast Marching Methods, Cambridge University Press, Cambridge, 1999.
[33] J. Sethian, J. Strain, Crystal growth and dendritic solidification, J. Comput. Phys. 98 (1992) 231–253.
[34] M. Sussman, P. Smereka, S. Osher, A level set approach for computing solutions to incompressible two-phase flow, J. Comput. Phys. 114 (1994) 146–159.
[35] H. Udaykumar, H. Mittal, W. Shyy, Computation of solid–liquid phase fronts in the sharp interface limit on fixed grids, J. Comput. Phys. 153 (1999) 535–574.
[36] J. Villain, J. Phys. 1 (1991).
[37] D. Xiu, G. Karniadakis, A semi-Lagrangian high-order method for Navier–Stokes equations, J. Comput. Phys 172 (2001) 658–684.